



Long-term stable optical cavity for special relativity tests in space

JOSEP SANJUAN,^{1,*} KLAUS ABICH,¹ MARTIN GOHLKE,¹ ANDREAS RESCH,¹ THILO SCHULDT,¹ TIMM WEGEHAUPT,¹ GEOFFREY P. BARWOOD,³ PATRICK GILL,³ AND CLAUS BRAXMAIER^{1,2}

¹German Aerospace Center (DLR), Robert-Hooke-Str. 7, Bremen 28359, Germany

²Center of Applied Space Technology and Microgravity (ZARM), University of Bremen, Am Fallturm 1, 28359 Bremen, Germany

³National Physical Laboratory (NPL), Hampton Road, Teddington, Middlesex, TW11 0LW, UK

*jose.sanjuan@dlr.de

Abstract: BOOST (BOOst Symmetry Test) is a proposed space mission to search for Lorentz invariance violations and aims to improve the Kennedy-Thorndike parameter constraint by two orders of magnitude. The mission consists of comparing two optical frequency references of different nature, an optical cavity and a hyperfine transition in molecular iodine, in a low Earth orbit. Naturally, the stability of the frequency references at the orbit period of 5400 s ($f=0.18$ mHz) is essential for the mission success. Here we present our experimental efforts to achieve the required fractional frequency stability of $7.4 \times 10^{-14} \text{ Hz}^{-1/2}$ at 0.18 mHz (in units of the square root of the power spectral density), using a high-finesse optical cavity. We have demonstrated a frequency stability of $(9 \pm 3) \times 10^{-14} \text{ Hz}^{-1/2}$ at 0.18 mHz, which corresponds to an Allan deviation of 10^{-14} at 5400 s. A thorough noise source breakdown is presented, which allows us to identify the critical aspects to consider for a future space-qualified optical cavity for BOOST. The major noise contributor at sub-milli-Hertz frequency was related to intensity fluctuations, followed by thermal noise and beam pointing. Other noise sources had a negligible effect on the frequency stability, including temperature fluctuations, which were strongly attenuated by a five-layer thermal shield.

© 2019 Optical Society of America under the terms of the [OSA Open Access Publishing Agreement](#)

1. Introduction

Optical cavities are essential to many high sensitivity measuring techniques and experiments where lasers with high frequency stability are needed. The required fractional stability and the frequency range of interest are diverse and span from values close to (in units of the square root of the power spectral density, PSD) $10^{-17} \text{ Hz}^{-1/2}$ at short time scales in atomic clocks [1–6] to $10^{-13} \text{ Hz}^{-1/2}$ at long time scales in space based laser interferometers such as the future gravitational wave detector LISA (Laser Interferometer Space Antenna) [7], the LRI (Laser Ranging Interferometer) on GRACE Follow-On (Gravity Recovery and Climate Experiment Follow-On) [8,9] and the next generation of gravity field missions [10]. Applications in future GNSS (Global Navigation Satellite Systems) concepts [11,12] will also benefit from optical cavities exhibiting stability levels in the $10^{-15} \text{ Hz}^{-1/2}$ range at time scales of seconds. High-stability frequency references are also key elements for tests of fundamental physics such as detection of violations of Lorentz invariance [13–15] through Michelson-Morley (MM) [16,17] and Kennedy-Thorndike (KT) [18,19] experiments. Satellite missions STAR, mSTAR and BOOST [20–23] have been proposed for such purposes. BOOST consists of comparing two highly stable frequency references based on completely different mechanisms, i.e., an optical resonator and a hyperfine transition of molecular iodine [24,25] in a low-Earth orbit. The experiment in space has the potential of improving the KT parameter constraint, with respect to on-ground experiments, by up to two orders of magnitude since its value is proportional to

\vec{v}^2/c_0^2 where \vec{v} is the velocity of the cavity relative to the rest frame and c_0 the speed of light. The hyperfine transition of the iodine molecule is, at first order, independent of \vec{v} . Thus, the frequency of the beat signal between both references should be sensitive to Lorentz invariance violations, if any exists. A crude estimate of the required fractional frequency stability, $S_{\delta\nu/\nu}^{1/2}$, for a given KT parameter uncertainty, α_{KT} , is calculated as

$$S_{\delta\nu/\nu}^{1/2}(f_0) \lesssim \alpha_{KT} \frac{2|\vec{v}_{\odot}||\vec{v}_{SC}| \sqrt{T_{\text{meas.}}}}{c_0^2 SNR} \approx 3 \times 10^{-13} \text{ Hz}^{-1/2} \quad (1)$$

where $|\vec{v}_{\odot}| \approx 400 \text{ km s}^{-1}$ is the solar system (plus Earth) velocity with respect to the Cosmic Microwave Background (CMB) [26], $|\vec{v}_{SC}| \approx 7.5 \text{ km s}^{-1}$ is the spacecraft modulating velocity at the orbit period, 5400 s, $SNR=1$ is the signal-to-noise ratio and $T_{\text{meas.}}=365$ days is the measurement duration. The frequency stability is required at $f_0 = 1/5400 \text{ s} = 0.18 \text{ mHz}$. In Eq. (1) we have considered $\alpha_{KT} = 7.5 \times 10^{-10}$, which is about two orders of magnitude better than current values from ground experiments [19].

In this paper we describe the experimental efforts to achieve the frequency stability compatible with the BOOST requirement [23] using an optical cavity. It has been set to $7.4 \times 10^{-14} \text{ Hz}^{-1/2}$ at 0.18 mHz, which poses a serious challenge due to the very low frequency of interest. For comparison, the requirements of other cavities working in the low frequency range, e.g., the LRI [27,28], LISA [29] and the next generation of gravity field missions [30,31], are in the $10^{-10} \text{ Hz}^{-1/2}$ levels at 0.18 mHz, i.e., 1000 times less demanding.

The paper is organized as follows: Sec. 2 describes the cavity set-up, i.e., the actual resonator together with the locking scheme, its mechanical mount and thermal shields. The latter is described in detail in Sec. 3 together with an experimental characterization of its transfer function in the frequency domain and the determination of the zero-crossing coefficient of thermal expansion (CTE) of the cavities. Section 4 presents the frequency stability results together with a detailed noise sources breakdown. The results are compared to the requirements and assumptions made for the BOOST mission. The system is characterized in the frequency range from 1 μHz to 1 Hz since some of the findings might be of interest for other future missions and experiments. Conclusions and future prospects are given in Sec. 5.

2. Set-up description

An 8.7 cm cubic optical cavity based on the National Physical Laboratory (NPL) design [32] has been chosen as frequency reference. Its theoretical thermal noise limit [33,34] is $3.1 \times 10^{-16} f^{-1/2} \text{ Hz}^{-1/2}$ (3.7×10^{-16} in Allan deviation), which corresponds to $2.3 \times 10^{-14} \text{ Hz}^{-1/2}$ at 0.18 mHz—see Sec. 4, i.e., a factor of three below the BOOST requirement. The cavity spacer is made of ultra-low expansion (ULE) glass with fused silica mirrors with ULE compensation rings optically bonded to its ends to achieve a zero-crossing CTE around room temperature [35,36]. Dielectric coated mirrors ($\text{SiO}_2/\text{Ta}_2\text{O}_5$ layers deposited by ion beam sputtering) provide a finesse of $\sim 400\,000$. The ULE spacer is rigidly mounted by four supports in a tetrahedral configuration, which makes it insensitive to forces with a maximum coupling factor of $2.5 \times 10^{-10} 1/(\text{m s}^{-2})$ [32]. The cavity and its mount are surrounded by five layers of thermal shields described in Sec. 3. The outermost layer of the shields include active temperature stabilization by means of Peltier elements and negative temperature coefficient (NTC) thermistors. The system is enclosed in a vacuum chamber and kept at a pressure of 10^{-7} mbar using an ion getter pump. A breadboard rigidly connected to the vacuum chamber contains the optic components for mode matching and the Pound-Drever-Hall (PDH) frequency stabilization technique [37]. A second breadboard with photodetectors for intensity stabilization is placed in the cavity's transmission port. An external breadboard contains a 1064 nm non-planar ring oscillator (NPRO) laser with two frequency actuators (piezo and crystal temperature), an electro-optical modulator (EOM)

for PDH side-bands generation, a voltage controlled optical attenuator for intensity stabilization and a pick-off for a beat measurement. The connections between the breadboards are done via optical fibers. The frequency and intensity stabilization control loops are implemented in a field programmable gate array (FPGA) together with 16-bit analog-to-digital converters (ADCs) and digital-to-analog converters (DACs) operating at a sampling frequency of ≈ 650 kHz. The set-up is replicated to be able to characterize one against each other by means of beat measurements. A drawing, photos of the cavity and the thermal shields and a schematic of the set-up are shown in Fig. 1.

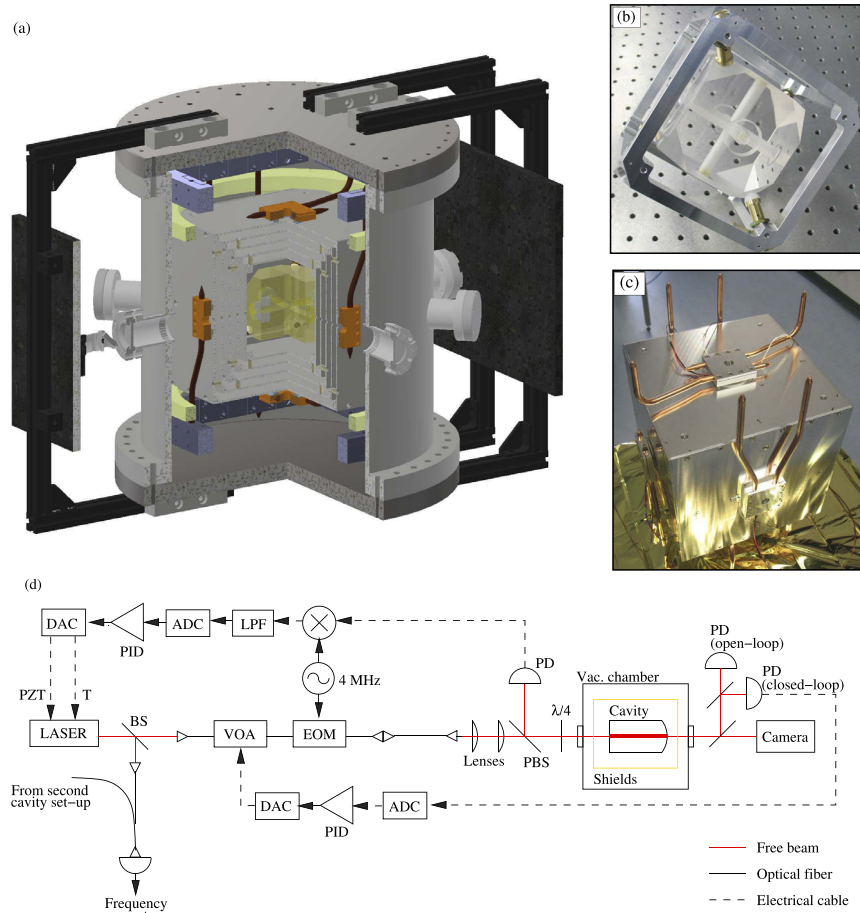


Fig. 1. (a) Drawing of the set-up. It includes the vacuum chamber, the five-layer thermal shields and the 8.7 cm cube cavity. The outermost shield includes Peltier elements that are connected to the vacuum chamber through heat pipes. The breadboards in the front and the back contain the input optics and the photodetectors in transmission (not shown for clarity), respectively. (b) 8.7 cm ULE cavity and tetrahedral mount. (c) Outermost thermal shield layer with Peltier elements (covered by adapters) and heat pipes. (d) PDH frequency stabilization scheme. ADC: analog-to-digital converter. BS: beam-splitter. DAC: digital-to-analog converter. EOM: electro-optical modulator. LPF: low-pass filter. PBS: polarizing beam-splitter. PD: photodetector. PID: proportional-integral-derivative controller. VOA: variable optical attenuator. $\lambda/4$: quarter wavelength plate.

3. Thermal shields design and characterization

Temperature fluctuations are one of the largest sources of technical noise at frequencies below the milli-Hertz level because they induce cavity length fluctuations due to the CTE. Consequently, the design of the thermal shields is crucial to reach frequency stability close to the thermal noise limit at 0.18 mHz. The required attenuation is calculated as:

$$|H_{TS}(f)| \leq \frac{1}{\alpha} \frac{S_{v,\text{req.}}^{1/2}(f)}{S_{T_0}^{1/2}(f)} \quad (2)$$

where $S_{T_0}^{1/2}$ and $S_{v,\text{req.}}^{1/2}$ are the thermal shields outermost layer temperature fluctuations and the relative frequency fluctuations requirement expressed as the square root of their PSDs, respectively. α is the effective CTE of the cavity. Following a conservative approach, the shields were designed assuming a CTE of $\alpha \approx 10^{-7} \text{ K}^{-1}$, which is the expected one for the cavity without compensation rings [35]. The temperature control in the outermost layer allowed temperature stability levels of $1 \text{ mK Hz}^{-1/2}$ and the frequency fluctuations due to temperature effects were set to be 10 times below the fundamental thermal noise limit, i.e., $S_{v,\text{req.}}^{1/2} \leq 2.5 \times 10^{-15} \text{ Hz}^{-1/2}$. Such settings resulted in a required attenuation of $|H_{TS}| \leq 2.5 \times 10^{-5}$ at 0.18 mHz.

The thermal shields were designed taking into account radiative and conductive heat transfer without considering the damping effect of the cavity spacer itself [38]. The adopted design consisted of five 3 mm-thick aluminium layers separated by four 10 mm-long polyether ether ketone (PEEK) hollow cylinders (4 mm and 8 mm inner and outer diameters, respectively) on each side in order to be mechanically stiff and withstand vibration and shock tests. The shields have apertures 5 mm in diameter for the laser beam to reach and leave the cavity. The outermost layer is a 236 mm cube and includes a Peltier element and NTC thermistors on each of the six sides. The Peltier elements used the vacuum chamber as a heat sink through a set of heat pipes as shown in Fig. 1. Large temperature changes (between $+10^\circ\text{C}$ and $+50^\circ\text{C}$) in the outermost layer were possible, which were convenient to determine the shields transfer functions and the zero-crossing CTE temperature —see Sec. 3.1.

Unlike in previous works [39,40], the thermal shields were characterized in the frequency domain by applying sine sweep signals in the outermost layer. The signals exhibited a wide spectrum spanning from about $1 \mu\text{Hz}$ to 1 mHz. The transfer function between the outermost layer and the j -th layer was calculated as:

$$H_{0 \rightarrow j}(f) = \frac{T_j(f)}{T_0(f)}, \quad j = 1, 2, \dots, 5 \quad (3)$$

where $T_j(f)$ is the Fourier transform of the temperature measured at the j -th layer. Note that $j = 5$ corresponds to the actual cavity. However, the transfer functions for the inner layers could not be measured for frequencies higher than tens of μHz . The reason was not the lack of SNR but the thermal leakage through the electrical cables to the actual temperature sensor head. Such limitation is shown in the dashed gray traces in Fig. 2 (top), which correspond to the heat transfer function of the sensors' cables. In order to measure the overall transfer function, $H_{0 \rightarrow 5}(f)$, at higher frequencies, the ULE cavity was replaced by an exact replica made of aluminium alloy 7075, which has a well-known and large CTE at room temperature ($\alpha_{\text{Al}} = 23.5 \times 10^{-6} \text{ K}^{-1}$ [41]), and thus can be used as a temperature sensor [39,42]. The 1064 nm laser was locked to the aluminium cavity using the set-up shown in Fig. 1. A second laser with 1064 nm and 532 nm outputs was locked to a hyperfine transition of the iodine molecule near 532 nm. A beat measurement was established between the lasers. Its frequency is proportional to temperature changes in the cavity provided temperature dominates the measurement. This was the case due to the large aluminium CTE, the large induced temperature variations and the excellent frequency

stability at long time scales of the unperturbed hyperfine transition of the iodine molecule. The transfer function was estimated as

$$H_{0 \rightarrow 5}(f) = \frac{1}{\alpha_{\text{Al}} \nu_0} \frac{\nu(f)}{T_0(f)} \quad (4)$$

where ν_0 and ν are the absolute laser frequency (≈ 282 THz) and the Fourier transform of the beat frequency, respectively. As a measurement validation, the aluminium cavity CTE was inferred by comparing the read-out of a thermistor glued to the aluminium cavity with the beat signal in the very low frequency regime ($\sim \mu\text{Hz}$). Its value was $24.2 \times 10^{-6} \text{ K}^{-1}$, which is within 3% of the expected one.

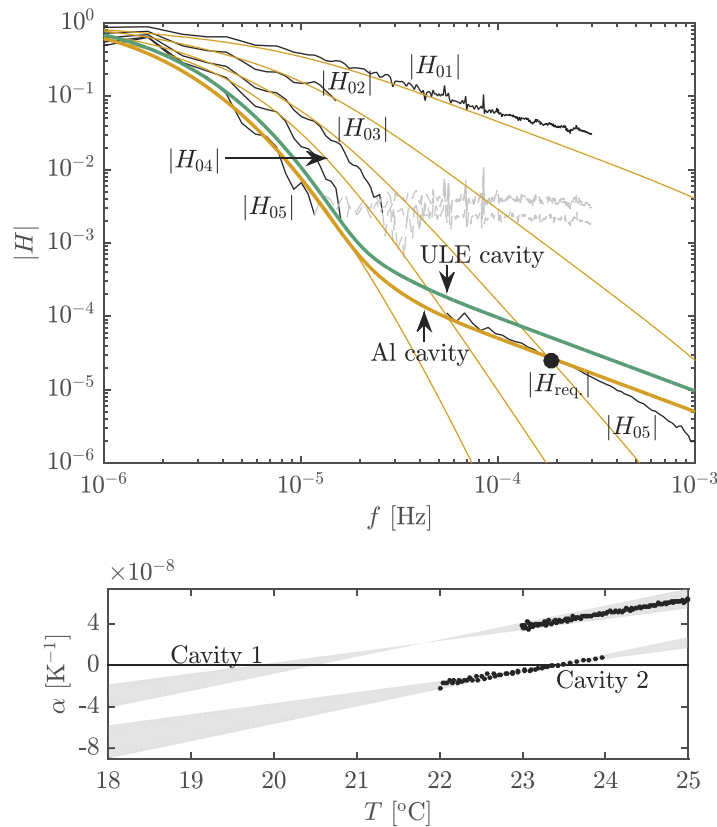


Fig. 2. Top: transfer functions of the layers of the thermal shields. Bottom: coefficient of thermal expansion. The zero-crossing temperatures are $(20 \pm 0.35)^\circ\text{C}$ and $(23.4 \pm 0.03)^\circ\text{C}$ for each cavity, respectively. The larger uncertainty in the former is due to the extrapolation needed since the actual zero-crossing temperature was not reached by the temperature sweep.

The transfer functions are shown in Fig. 2 (top). Black lines correspond to experimental values. Temperature sensors provided values from $2 \mu\text{Hz}$ to $30 \mu\text{Hz}$ for $H_{0 \rightarrow 3,4,5}$ and up to $300 \mu\text{Hz}$ for the first layer, $H_{0 \rightarrow 1}$. The thermistor in the second layer exhibited a faulty behavior that prevented us to measure above $20 \mu\text{Hz}$. Ochre traces are the fits using the model described in [38]. The free parameters of the fits were the aluminium emissivity and the PEEK thermal conductivity. Their values were in good agreement with the theoretical ones (0.05 and $0.2 \text{ W m}^{-1} \text{ K}^{-1}$ for the emissivity and thermal conductivity, respectively). The black trace between $70 \mu\text{Hz}$ and 1 mHz corresponds to the transfer function measured using the aluminium cavity and, clearly, does not

agree with the expected one. This is likely due to the apertures in the shields, which constitute a direct thermal link between the outermost layer and the cavity. An aperture is defined here as the holes in thermal shields layers to allow the laser beam to reach the cavity. Typically, there are always two apertures per cavity, i.e., for the input and the transmitted beam. The thermal link can be modeled as a first-order low-pass filter with a cut-off frequency of $f_c = \frac{1}{2\pi\theta C}$ where θ and C are the radiative thermal resistance between the outermost layer and the cavity and the cavity thermal capacitance, respectively. The latter is $C = mc_s$ with m the mass of the cavity and c_s the specific heat of the aluminum. The former is

$$\theta \simeq \frac{1}{4N\pi r^2 \sigma_{SB} T^3} \left(\frac{1 - \epsilon_{sh}}{\epsilon_{sh}} + \frac{1}{F} + \frac{1 - \epsilon_{cav}}{\epsilon_{cav}} \right) \quad (5)$$

where N , r , T , σ_{SB} , ϵ_{sh} and ϵ_{cav} are the number of apertures, the radius of the apertures, the absolute temperature in Kelvin, the Stefan-Boltzmann constant and the emissivity of the shields and cavity, respectively. F is the view factor from the outermost layer to the cavity, which can be approximated by the view factor between coaxial parallel disks separated by a distance ℓ [43]:

$$F \simeq \frac{1}{2} \left\{ 2 + \ell^2/r^2 [1 - (1 + 4r^2/\ell^2)^{1/2}] \right\}. \quad (6)$$

In our case $\ell=0.0575$ m and $r=2.5$ mm, which yields a view factor of $F=0.0075$. The thermal resistance is $\sim 3 \times 10^5$ K W⁻¹ and the thermal capacitance is 1600 J K⁻¹, which results in a cut-off frequency in the nano-Hertz range. The shields plus apertures transfer function is shown by the thick ocher trace in Fig. 2 (top). The discrepancy above 500 μ Hz is due to the simplicity of the model that does not consider faster responses of the system such as the compensation rings and mirrors. The thick teal line represents the expected transfer function when using the ULE cavity, which is different from the aluminium one due to differences in the thermal mass, C , and the emissivity, ϵ_{cav} . The characterization of the shields in the frequency domain shows clearly the importance of the apertures at frequencies above the cut-off frequency of the shields. The effect of the apertures can be minimized by reducing their size. In our case the minimum size is $r=1.25$ mm since the beam waist is 300 μ m, which implies a 15-fold improvement in attenuation. Another possibility mentioned in [23] is the use of BK7 glass in the apertures to reduce the radiation link. Instead, we tried short-pass optical filters with a cut-off wavelength of 1100 nm to reduce long-wavelength infrared (tens of μ m). However, this only led a two-fold increase in attenuation.

In summary, Fig. 2 (top) shows the thermal shields attenuation is slightly above the required value due to the presence of the apertures. However, the requirement was set under very conservative assumptions and as shown in Sec. 4 temperature fluctuations did not have any impact in the cavity stability for $f > 10$ μ Hz. The results also show that the two innermost layers are unnecessary since they are by-passed by the apertures thermal link. Its suppression will reduce the size of the shields from 236 mm cube to 165 mm cube and the mass including the ULE cavity from 3 kg to 2.1 kg, which is always beneficial for space missions. This approach will reduce ℓ in Eq. (6) and degrade the shields attenuation by a factor of two. However, the original attenuation levels can be recovered by reducing the size of the apertures by a 15%.

3.1. Zero-crossing coefficient of thermal expansion

Further mitigation of temperature fluctuations was enabled by determining the cavity (ULE spacer with fused silica mirrors and compensation rings —see Sec. 2) zero-crossing CTE temperature. To do so a 10 K sine wave modulation at a frequency of 2.8 μ Hz was applied at the outermost layer of the shields. The temperature sensor in the innermost thermal shield layer measured an amplitude of about 1.5 K. Simultaneously, the frequency of the beat signal between the ULE

cavity and the laser locked to the hyperfine transition of the iodine molecule was measured and converted to length changes. The CTE was calculated as

$$\alpha(T) = \frac{1}{\ell_0} \frac{d\Delta\ell(T)}{dT(T)} \quad (7)$$

where $\ell_0=8.7$ cm is the length of the cavity, $\Delta\ell$ are the cavity length changes and ΔT is the temperature of the cavity. The latter was inferred from the sensor in the innermost thermal shield layer by applying the transfer function from the last thermal shield layer to the cavity, $H_{4\rightarrow 5}(f)$. The CTEs are shown in Fig. 2 (bottom) for both cavities. The confidence intervals are mostly due to the transfer function uncertainty between the innermost shield layer and the cavity, which becomes larger for set-up 1 due to the need for extrapolation. The temperature working points were set to the zero-crossing ones, i.e., 20°C and 23.4°C for each cavity, respectively. They were kept at these temperatures within ± 50 mK using the active temperature control in the outermost layer. This allowed us to ensure the CTE was always $\lesssim 10^{-8}$ K⁻¹. The CTE temperature dependence is around 1.3×10^{-8} K⁻², which indicates that the requirement in the zero-crossing CTE temperature is not very demanding. For instance, ± 1 K uncertainty causes the CTE to be within $\pm 1.3 \times 10^{-8}$ K⁻¹, which combined with the thermal shields attenuation and active temperature control is sufficient to keep temperature effects negligible. This relaxes significantly the values assumed for the BOOST mission [23], where the requirement for the working temperature is set to 10 mK. Obviously, reducing the zero-crossing temperature uncertainty implies less demanding thermal attenuation. However, working at the zero-crossing temperature within values smaller than ± 50 mK seems unlikely due to the uncertainty in the zero-crossing point and temperature fluctuations at long time scales. Finally, the temperature fluctuations allowed in the spacecraft platform can be estimated as

$$S_{T_{sc}}^{1/2}(f) \lesssim \frac{S_{\delta\nu/\nu,T}^{1/2}(f)}{\alpha|H_{0\rightarrow 5}(f)|} |H_{CL}(f)| \sim 15 \text{ K Hz}^{-1/2} \text{ at } f = 0.18 \text{ mHz}, \quad (8)$$

where $S_{\delta\nu/\nu,T}^{1/2}$ is the allowed frequency noise caused by temperature fluctuations ($\simeq 7.4 \times 10^{-15}$ Hz^{-1/2}), α has been assumed 10^{-8} K⁻¹ and $|H_{0\rightarrow 5}(f)| = 5 \times 10^{-5}$. $|H_{CL}(f)|$ is the open-loop gain at 0.18 mHz of the temperature control provided by the Peltier elements in the outermost layer, which can be about 1000. Note that $15 \text{ K Hz}^{-1/2}$ represents peak-to-peak variations of ~ 0.5 K in time scales of the orbit period, 5400 s.

4. Stability results and noise sources

The fractional frequency stability between the two cavities is shown in the top panel of Fig. 3 in units of the square root of the PSD. The results have been scaled by a factor of $1/\sqrt{2}$, i.e., they represent the stability of one set-up assuming their noise sources are similar and uncorrelated. At 0.18 mHz, the value is $(8.9 \pm 3.2) \times 10^{-14}$ Hz^{-1/2}, which is very close to the BOOST requirement, 7.4×10^{-14} Hz^{-1/2}. For completeness, the Allan deviation is shown in the bottom panel. The solid red trace was calculated after subtracting an exponential fit to the time-domain data, which corresponds to ULE creep —see Sec. 4.7. The dashed red trace was calculated after applying a linear detrend to the original time-domain data. The values at 5400 s are 10^{-14} and 1.5×10^{-14} for both detrending approaches, respectively. The top plot in Fig. 3 also shows the contribution of different sources of noise on the frequency stability. The total amount is represented by the purple trace, which fails to explain the frequency noise between 20 μ Hz and 700 μ Hz. This discrepancy is discussed in Sec. 4.9 and is likely related to intensity fluctuations. For $f > 3$ mHz the stability can be explained by mirrors' coating thermal noise and optical fibers noise.

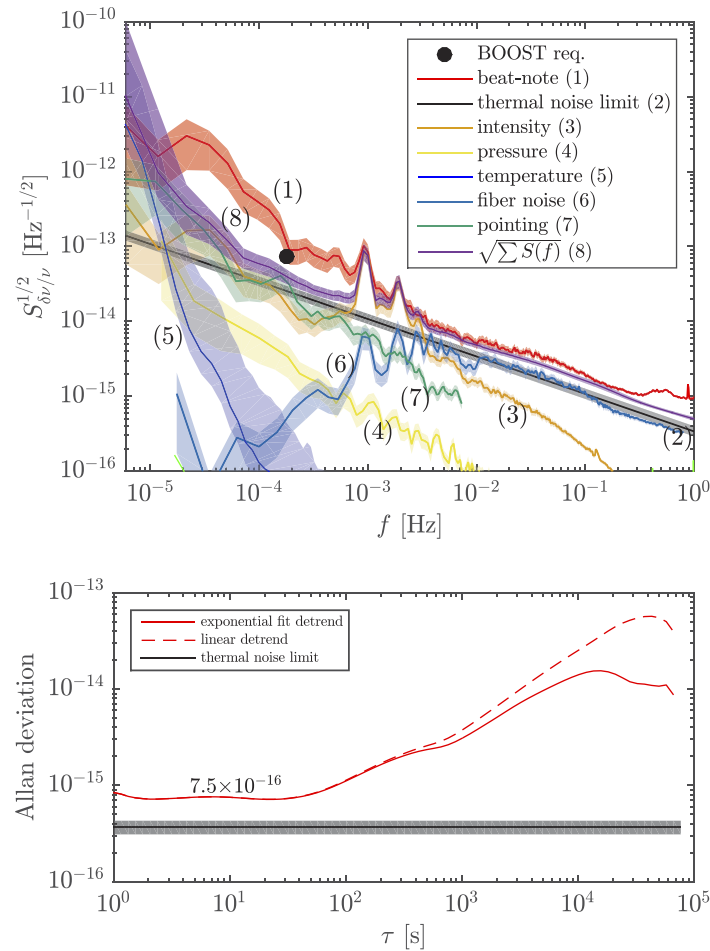


Fig. 3. Top: the red trace is the fractional frequency stability as the square root of the PSD, which is at the BOOST requirement level. The purple trace is the root sum squared of all the sources of noise, which, clearly, cannot explain the frequency noise in the 50 μHz to 700 μHz band. Bottom: fractional frequency stability expressed in Allan deviation after exponential fit subtraction (solid red trace) and linear detrend (dashed red trace).

4.1. Thermal noise

Thermal noise is the fundamental frequency stability limit in a rigid cavity [33,34,36]. In our case the mirrors' dielectric coatings thermal noise is the dominating one. Its expression is

$$S_{\delta\nu/\nu}^{1/2}(f) = \left(2 \frac{4k_{\text{B}}T}{2\pi f} \frac{2(1+\sigma)(1-2\sigma)}{\pi E} \frac{d}{w^2} \phi \right)^{1/2} / \ell \quad (9)$$

where $E = 73 \text{ GPa}$ is the Young's modulus of the mirror's substrate, $d = 5.3 \mu\text{m}$ is the coating's thickness, $w = 315 \mu\text{m}$ is the beam size at the mirrors, $\sigma = 0.17$ is the Poisson's ratio of fused silica, $\phi = 4 \times 10^{-4}$ is the coating's loss-angle and $\ell = 8.7 \text{ cm}$ the spacer's length. k_{B} is the Boltzmann constant and T is the absolute temperature, 300 K. Evaluation of Eq. (9) yields $(3.2 \pm 0.5) \times 10^{-16} f^{-1/2}$ (black straight line in Fig. 3), where the confidence intervals have been calculated considering small uncertainties in some of the parameters. In terms of Allan deviation, it is equivalent to $(3.7 \pm 0.6) \times 10^{-16}$ for any integration time. The frequency stability of the

cavities is a factor 1.7 higher than the thermal noise limit at frequencies between 3 mHz and 0.3 Hz. For $f < 3$ mHz, the stability increases as f^{-1} and at 0.18 mHz is 3.5 times higher than the thermal noise limit.

4.2. Intensity fluctuations

Intensity fluctuations cause temperature variations in the mirrors surface that translate into thermoelastic deformations that change the effective length of the cavity [44]. The coupling factor between intensity and frequency was measured by applying sweep sines and step functions in one of the cavities while measuring the beat frequency simultaneously. The measurements were performed at different input levels spanning from 20 μW to 140 μW with amplitude modulations of 5 μW . The resulting transfer function for one of the cavities was

$$H_I(f) \approx 90 \frac{1}{i \frac{f}{0.04} + 1} \frac{1}{i \frac{f}{0.85} + 1} \quad [\text{Hz } \mu\text{W}^{-1}]. \quad (10)$$

For the second cavity similar results were obtained: $\approx 115 \text{ Hz } \mu\text{W}^{-1}$ and 42 mHz and 1 Hz. These coupling factors are in very good agreement with theoretical predictions [44] and similar to the ones assumed for the BOOST mission: 100-200 $\text{Hz } \mu\text{W}^{-1}$ [23,45]. Considering a coupling factor of 115 $\text{Hz } \mu\text{W}^{-1}$, the required intensity stability to meet the BOOST requirement is 180 $\text{nW Hz}^{-1/2}$, which for a transmitted power of 100 μW is equivalent to a relative intensity noise (RIN) of $1.7 \times 10^{-3} \text{ Hz}^{-1/2}$ at 0.18 mHz. This is orders of magnitude below the RIN of an NPRO and, thus, requires active intensity stabilization as described in Sec. 2. We measured the intensity stability by placing a beam-splitter and a second photodetector in the transmission port of the cavity —see Fig. 1. Thus, the out-of-loop stability was measured while keeping the cavity stabilized in both frequency and intensity. The fluctuations were 35 $\text{nW Hz}^{-1/2}$ at 0.18 mHz (RIN = $3.5 \times 10^{-4} \text{ Hz}^{-1/2}$), i.e., a factor of five better than the requirement. Their contribution is shown in Fig. 3 by the orange trace and, apparently —see Sec. 4.9, only limits the stability at frequencies of 1 mHz and 2 mHz where the two spikes are present.

4.3. Pressure fluctuations

Index of refraction fluctuations due to pressure cause effective length fluctuations in the cavity, which, in turn, degrade the frequency stability, i.e.,

$$S_{\delta\nu/\nu}^{1/2}(f) = S_{\delta n}^{1/2}(f) = |H_p(f)| S_p^{1/2}(f) \quad (11)$$

where $|H_p|$ is the transfer function between pressure and frequency (or index of refraction), which was measured by applying a sudden change in the pressure and resulted in

$$H_p(f) = 50 \frac{1}{i \frac{f}{0.05} + 1} \quad [\text{Hz nbar}^{-1}]. \quad (12)$$

The other chamber exhibited again very similar values: 45 Hz nbar^{-1} coupling factor and a corner frequency of 0.08 Hz. The index of refraction of nitrogen (assumed as the main residual gas in the chamber) is about $3 \times 10^{-13} \text{ nbar}^{-1}$ at $p = 10^{-7} \text{ mbar}$. Our measurement was slightly different, $1.8 \times 10^{-13} \text{ nbar}^{-1}$ ($= 50 \text{ Hz nbar}^{-1} / 282 \text{ THz}$), which was likely due to different pressure levels between the actual vacuum gauge and the cavity [46]. According to Eq. (12) the pressure fluctuations must be less than 0.4 $\mu\text{bar Hz}^{-1/2}$ to meet the BOOST requirement. This was comfortably met by keeping the vacuum chamber at a pressure of 10^{-7} mbar with ion-getter pumps. The yellow trace in Fig. 3 shows the pressure fluctuations converted to frequency. Clearly, its contribution is negligible. The BOOST mission requirement was set to 10^{-8} mbar . However, according to these results it could be relaxed to 10^{-7} or 10^{-6} mbar .

4.4. Temperature fluctuations

The contribution of temperature fluctuations to the frequency stability is shown by the blue trace in Fig. 3. They were measured at the outermost layer of the shields by out-of-loop sensors and, subsequently, the shields transfer function was applied to it to estimate the fluctuations in the cavity. The last step consisted of using the cavity's CTE to calculate the equivalent frequency stability. The CTEs were chosen between 10^{-9} K^{-1} and $2 \times 10^{-8} \text{ K}^{-1}$ in order to cope with uncertainties and is shown by the wide blue band in Fig. 3. The dark blue trace within the blue band corresponds to a CTE of 10^{-9} K^{-1} and shows that they only become relevant for frequencies below $20 \mu\text{Hz}$. At 0.18 mHz the contribution is about three orders of magnitude below the BOOST requirement, which indicates that the shields can be significantly downsized as suggested in Sec. 3.

4.5. Beam pointing fluctuations

The beam sent to the cavity was subjected to pointing jitter due to laboratory vibrations and, in our case, more importantly due to slow temperature variations that distort the position of the beam with respect to the cavity. Beam pointing misalignment includes four degrees of freedom: two transverse positions and two angular tilts. Small variations of any of these degrees of freedom have an impact in the performance of the cavity. The coupling coefficients were determined by applying misalignments while measuring the beat and ensuring the intensity was kept constant. The set-up to measure it consisted of a beam-splitter in front of the input mirror of the cavity with a charged-couple device (CCD) camera in the reflective port, which allowed us to monitor the beam position while keeping the cavity locked. The beam-pointing to frequency stability coefficient was $\sim 0.5 \text{ Hz } \mu\text{m}^{-1}$ where μm refers to the position of the beam in the CCD camera either due to tilt or lateral shift. We also changed the position and size of the beam waist by using translation stages that allowed us to change them independently. The effect was found to be negligible. The beam pointing contribution is shown by the green trace in Fig. 3, which is at the thermal noise limit for $f < 1 \text{ mHz}$.

4.6. Fiber noise

In our setup the laser head, the EOM, the variable optical attenuator, the beat measurement, etc. were placed in a breadboard separated from the vacuum chamber and the input optics breadboards—see Fig. 1. The connection between the breadboards was done through three meter long optical fibers. Phase noise, $S_{\phi}^{1/2}$, induced in the fibers due to laboratory temperature, vibrations and acoustics translates into frequency noise as $S_{\delta\nu}^{1/2} = 2\pi f S_{\phi}^{1/2}$, which is largely attenuated at low frequencies since the effect is proportional to the Fourier frequency, f . The noise contribution is shown by the blue trace in Fig. 3 where the high-pass filter behavior is clearly seen and becomes negligible below 1 mHz . However, at higher frequencies it dominates the fluctuations together with the thermal noise. Fiber stabilization techniques [47,48], shorter fibers or free space setups were not contemplated since the effect at the BOOST frequency was not relevant.

4.7. Long-term drifts

The beat frequency rate was also monitored at different times after the installation of the cavities in the vacuum chambers by comparing the cavities to the laser locked to the hyperfine line of the molecule iodine. The response followed an exponential response, or

$$\dot{\nu}(t) = \frac{\Delta\nu}{\tau} e^{-t/\tau}, \quad (13)$$

where $\Delta\nu = 5 \pm 0.5 \text{ MHz}$ and $\tau = 205 \pm 19 \text{ day}$. This corresponds to frequency rates starting at 300 mHz s^{-1} and reducing to 40 mHz s^{-1} after 415 days. Such drift does not have any impact in the frequency stability at 0.18 mHz since its energy is concentrated at much lower frequencies.

4.8. Others

Here we summarize noise sources of different nature. Noise coming from phase fluctuations between the EOM modulating and demodulating signals that generate the PDH error signal had a negligible impact in the overall stability as opposed to the rather large contribution assumed for BOOST [23]. The coupling coefficient was $\sim 60 \text{ Hz rad}^{-1}$. The gain limitation of the feedback control had also a negligible contribution below 100 mHz. The noise due to laser RIN and photodetector noise at the modulating frequency (few MHz), together with associated amplifiers and ADCs was found to be white noise below $10^{-17} \text{ Hz}^{-1/2}$ and in good agreement with the expected values. Residual amplitude modulation (RAM) [49–51] did not have any effect in the measurement due to the high finesse of the cavity together with the fiber coupled EOMs with very small RAM and tilted/wedged optics.

4.9. Intensity fluctuations revisited

As shown in Fig. 3, the noise sources considered previously failed to explain the frequency stability between 20 μHz and 700 μHz . This suggests that the beat frequency should not correlate with any of them. We tested this assumption by calculating the coherence function, $\gamma(f)$. The results are shown in Figs. 4(a) and (b) and, surprisingly, rather large values were present for the out-of-loop intensity signal between 20 μHz and 200 μHz (the large values at 1 mHz and 2 mHz peaks were expected). This finding justifies the estimation of the transfer function between intensity and frequency as

$$|H_{I^*}(f)| = \frac{S_{\delta v}^{1/2}(f)}{S_{\delta I}^{1/2}(f)}, \quad (14)$$

where H_{I^*} is different from H_I since the latter was estimated with high SNR —see Sec. 4.2, while the former was obtained from a quiet run. The uncertainty in $|H_{I^*}|$ is related to the coherence function as [52]

$$\sigma_{|H_I|}(f) = \frac{\sqrt{1 - \gamma^2(f)}}{\gamma(f)\sqrt{2n}}, \quad (15)$$

where n is the number of averages used to calculate γ . Equation (15) indicates that small γ values imply poor transfer function estimation. This is clearly seen in Fig. 4(c), where the other trace shows the transfer function calculated from Eq. (14) and exhibits large uncertainties where the coherence function is small. Anyhow, the coupling in the 50 μHz to 5 mHz is well estimated and at 0.18 mHz is $\sim 1 \text{ kHz } \mu\text{W}^{-1}$, which is 10 times larger than the one described in Sec. 4.2 [red and black traces in Fig. 4(c)]. The *new* coupling coefficient was also calculated by comparing the root mean square (RMS) intensity and beat frequency fluctuations in the 50 μHz to 500 μHz band. This was done by calculating the PSD and, subsequently, the RMS values of moving short-time windows. The results are shown in Fig. 4(d) where the coupling was found to be $(1.5 \pm 0.2) \text{ kHz } \mu\text{W}^{-1}$. The plot also reveals that frequency and intensity fluctuations are not completely stationary at such frequencies, probably due to changing laboratory conditions, which are difficult to keep stable during days.

The puzzling discrepancy between the transfer functions can be explained by the underestimation of the intensity fluctuations in the cavity due to a common noise source, e.g., temperature fluctuations. Intensity fluctuations are inferred from the out-of-loop photodetector in the cavity's transmission port —see Fig. 1, and can be expressed as

$$S_{\delta I, \text{PD}_{\text{out-of-loop}}}^{1/2}(f) \simeq \Delta\alpha_{\text{PD}} P_{\text{cav}} S_T^{1/2}(f) \quad (16)$$

where $\Delta\alpha_{\text{PD}}$ is the in-loop and out-of-loop photodetectors' responsivity temperature coefficient mismatch, P_{cav} is the cavity's input power ($\sim 100 \mu\text{W}$) and $S_T^{1/2}$ the photodetectors' temperature

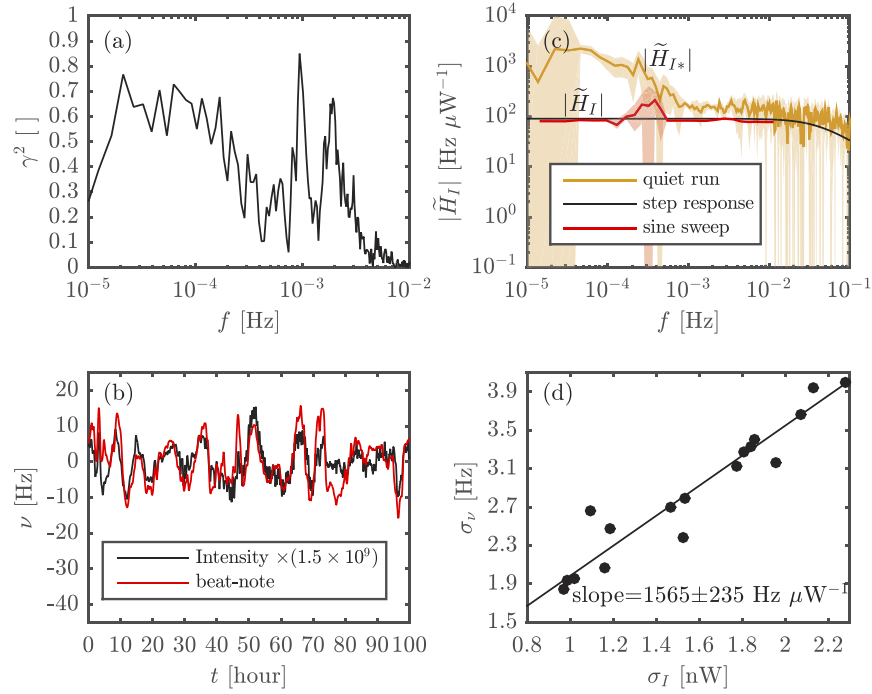


Fig. 4. (a) Coherence function between beat signal and transmitted intensity measured by the out-of-loop photodetector. (b) Beat-note and transmitted intensity in the time domain after band-pass filtering between $5 \mu\text{Hz}$ and $500 \mu\text{Hz}$. (c) Other trace is the transfer function calculated using Eq. (14). The red and black traces are the ones estimated using large SNR —see Sec. 4.2. (d) RMS values of intensity and frequency fluctuations in the $50 \mu\text{Hz}$ to $500 \mu\text{Hz}$ band. The data points correspond to the RMS values of moving short-time windows.

fluctuations. However, the actual intensity fluctuations in the cavity are

$$S_{\delta I, \text{cav}}^{1/2}(f) \approx |\alpha_{\text{PD, in-loop}} + \beta| P_{\text{cav}} S_T^{1/2}(f) \quad (17)$$

where $\alpha_{\text{PD, in-loop}}$ is the in-loop photodetector temperature coefficient and β represents a temperature coefficient that includes mechanisms affecting the transmitted intensity from the cavity to the photodetectors, e.g., changes in polarization, in the transmissivity of the optical window, the beam-splitters, etc. From Eqs. (16) and (17), the transfer function calculated using Eq. (14) is related to the one estimated with high SNR by

$$|H_{I^*}(f)| = \left| \frac{\alpha_{\text{PD, in-loop}} + \beta}{\Delta\alpha_{\text{PD}}} \right| |H_I(f)|, \quad (18)$$

which can easily lead to an amplification of $|H_I(f)|$, especially with photodetectors with similar temperature coefficients. Furthermore, from Eq. (17) and $S_{\delta\nu/\nu}^{1/2}$ the value of $|\alpha_{\text{PD, in-loop}} + \beta|$ has been estimated to be $\sim 3 \times 10^{-3} \text{ K}^{-1}$, which is in the same order of InGaAs photodetectors responsivity temperature coefficients alone [53]. In this case Fig. 4 suggests that intensity fluctuations contribute significantly to the frequency stability in the $20 \mu\text{Hz}$ to 2 mHz range, as opposed to the first estimations shown in Sec. 4.2 and that a two-fold reduction is needed to meet the BOOST requirement. However, other noise sources cannot be completely ruled out. For instance, frequency fluctuations due to large polarization fluctuations [54] in the cavity

together with the polarization dependence on the splitting ratio of the beam-splitter in front of the photodetectors could lead to similar results. In such scenario, intensity fluctuations are an excellent proxy of the problem but its reduction would not improve the frequency stability of the set-up.

5. Summary

We have shown a fractional frequency stability in units of the square root of the PSD of $(9\pm 3)\times 10^{-14} \text{ Hz}^{-1/2}$ at 0.18 mHz, which is at the BOOST requirement level, $7.4\times 10^{-14} \text{ Hz}^{-1/2}$. The Allan deviation at 5400 s was $\approx 10^{-14}$. For frequencies above 3 mHz the stability was $5\times 10^{-16}/f^{1/2}$ (in the square root of the PSD) and 7.5×10^{-16} for $\tau < 100$ s (in Allan deviation) and can be explained by mirrors' coating thermal noise and optical fibers noise.

The limiting noise source in the 20 μHz to 2 mHz band have been primarily attributed to intensity fluctuations that were initially undervalued due to common mode fluctuations cancellation between the out-of-loop and the in-loop photodetectors in the cavity transmission port. A two-fold reduction of intensity coupling into frequency stability would suffice to meet the BOOST requirement. Several options are foreseen to do so, e.g., reducing the input power in the cavity, including active temperature stabilization in the photodetectors and placing them inside the vacuum chamber. However, other noise sources such as polarization fluctuations could also be responsible for the low-frequency noise, which would not benefit for better intensity stabilization or less input power. The other sources of noise slightly below the requirement are mirrors' coating thermal noise and beam pointing stability. The former is, by design, below the BOOST requirement, while the latter should be strongly suppressed in a robust and compact space-like input optics design.

Another outcome of this work has been the determination of the thermal shields transfer function and the zero-crossing CTE temperature, which are important to keep temperature fluctuations well below the requirement. The shields exhibited an attenuation of $\sim 5\times 10^{-5}$ at 0.18 mHz, and was limited by the apertures for the laser beam to reach the cavity, which suggests that at least two layers can be eliminated without degrading attenuation capability. The small CTE temperature dependence indicates that operating at a temperature ± 1 K around the zero-crossing CTE should be sufficient to keep temperature effects negligible at 0.18 mHz.

Funding

Bundesministerium für Wirtschaft und Technologie (50QT1401); Helmholtz Association (ZT-0007); UK Space Agency; European Space Agency.

References

1. A. D. Ludlow, M. M. Boyd, J. Ye, E. Peik, and P. O. Schmidt, "Optical atomic clocks," *Rev. Mod. Phys.* **87**(2), 637–701 (2015).
2. N. Hinkley, J. A. Sherman, N. B. Phillips, M. Schioppo, N. D. Lemke, K. Beloy, M. Pizzocaro, C. W. Oates, and A. D. Ludlow, "An atomic clock with 10^{-18} instability," *Science* **341**(6151), 1215–1218 (2013).
3. B. J. Bloom, T. L. Nicholson, J. R. Williams, S. L. Campbell, M. Bishof, X. Zhang, S. L. Bromley, and J. Ye, "An optical lattice clock with accuracy and stability at the 10^{-18} level," *Nature* **506**(7486), 71–75 (2014).
4. S. Falke, N. Lemke, C. Grebing, B. Lipphardt, S. Weyers, V. Gerginov, N. Huntemann, C. Hagemann, A. Al-Masoudi, S. Häfner, S. Vogt, U. Sterr, and C. Lisdat, "A strontium lattice clock with 3×10^{-17} inaccuracy and its frequency," *New J. Phys.* **16**(7), 073023 (2014).
5. I. Ushijima, M. Takamoto, M. Das, T. Ohkubo, and H. Katori, "Cryogenic optical lattice clocks," *Nat. Photonics* **9**(3), 185–189 (2015).
6. L. Jin, Y. Jiang, Y. Yao, H. Yu, Z. Bi, and L. Ma, "Laser frequency instability of 2×10^{-16} by stabilizing to 30-cm-long Fabry-Pérot cavities at 578 nm," *Opt. Express* **26**(14), 18699–18707 (2018).
7. P. Amaro-Seoane, H. Audley, S. Babak, J. Baker, E. Barausse, P. Bender, E. Berti, P. Binetruy, M. Born, D. Bortoluzzi, J. Camp, C. Caprini, V. Cardoso, M. Colpi, J. Conklin, N. Cornish, C. Cutler, K. Danzmann, R. Dolesi, L. Ferraioli, V. Ferroni, E. Fitzsimons, J. Gair, L. Gesa Bote, D. Giardini, F. Gibert, C. Grimani, H. Halloin, G. Heinzel, T. Hertog, M. Hewitson, K. Holley-Bockelmann, D. Hollington, M. Hueller, H. Inchauspe, P. Jetzer, N. Karnesis, C. Killow,

- A. Klein, B. Klipstein, N. Korsakova, S. L. Larson, J. Livas, I. Lloro, N. Man, D. Mance, J. Martino, I. Mateos, K. McKenzie, S. T. McWilliams, C. Miller, G. Mueller, G. Nardini, G. Nelemans, M. Nofrarias, A. Petiteau, P. Pivato, E. Plagnol, E. Porter, J. Reiche, D. Robertson, N. Robertson, E. Rossi, G. Russano, B. Schutz, A. Sesana, D. Shoemaker, J. Slutsky, C. F. Sopena, T. Sumner, N. Tamanini, I. Thorpe, M. Troebs, M. Vallisneri, A. Vecchio, D. Vetrugno, S. Vitale, M. Volonteri, G. Wanner, H. Ward, P. Wass, W. Weber, J. Ziemer, and P. Zweifel, "Laser Interferometer Space Antenna," *arXiv e-prints* arXiv:1702.00786 (2017).
8. B. S. Sheard, G. Heinzel, K. Danzmann, D. A. Shaddock, W. M. Klipstein, and W. M. Folkner, "Intersatellite laser ranging instrument for the GRACE Follow-on mission," *J. Geod.* **86**(12), 1083–1095 (2012).
 9. K. Abich, A. Abramovici, B. Amparan, A. Baatzsch, B. B. Okiihiro, D. C. Barr, M. P. Bize, C. Bogan, C. Braxmaier, M. J. Burke, K. C. Clark, C. Dahl, K. Dahl, K. Danzmann, M. A. Davis, G. de Vine, J. A. Dickson, S. Dubovitsky, A. Eckardt, T. Ester, G. F. Barranco, R. Flatscher, F. Flechtner, W. M. Folkner, S. Francis, M. S. Gilbert, F. Gilles, M. Gohlke, N. Grossard, B. Guenther, P. Hager, J. Hauden, F. Heine, G. Heinzel, M. Herding, M. Hinz, J. Howell, M. Katsumura, M. Kaufer, W. Klipstein, A. Koch, M. Kruger, K. Larsen, A. Lebeda, A. Lebeda, T. Leikert, C. C. Liebe, J. Liu, L. Lobmeyer, C. Mahrtdt, T. Mangoldt, K. McKenzie, M. Misfeldt, P. R. Morton, V. Müller, A. T. Murray, D. J. Nguyen, K. Nicklaus, R. Pierce, J. A. Ravich, G. Reavis, J. Reiche, J. Sanjuan, D. Schütze, C. Seiter, D. Shaddock, B. Sheard, M. Sileo, R. Spero, G. Spiers, G. Stede, M. Stephens, A. Sutton, J. Trinh, K. Voss, D. Wang, R. T. Wang, B. Ware, H. Wegener, S. Windisch, C. Woodruff, B. Zender, and M. Zimmermann, "In-orbit performance of the GRACE Follow-on laser ranging interferometer," *Phys. Rev. Lett.* **123**(3), 031101 (2019).
 10. S. Dionisio, A. Anselmi, L. Bonino, S. Cesare, L. Massotti, and P. Silvestrin, "The next generation gravity mission: challenges and consolidation of the system concepts and technological innovations," in *2018 SpaceOps Conference*, (2018).
 11. C. Günther, "Kepler - satellite navigation without clocks and ground infrastructure," in *ION GNSS+ 2018*, (2018), pp. 849–856.
 12. G. Giorgi, T. Schmidt, C. Trainotti, R. Mata-Calvo, C. Fuchs, M. Hoque, J. Berdermann, J. Furthner, C. Günther, T. Schuldt, J. Sanjuan, M. Gohlke, M. Oswald, C. Braxmaier, K. Balidakis, G. Dick, F. Flechtner, M. Ge, S. Glaser, R. König, G. Michalak, M. Murböck, M. Semmling, and H. Schuh, "Advanced technologies for satellite navigation and geodesy," *Adv. Space Res.* **64**(6), 1256–1273 (2019).
 13. J. D. Tasson, "What do we know about lorentz invariance?" *Rep. Prog. Phys.* **77**(6), 062901 (2014).
 14. C. Lämmerzahl, H. Dittus, A. Peters, and S. Schiller, "OPTIS: a satellite-based test of special and general relativity," *Classical Quantum Gravity* **18**(13), 2499–2508 (2001).
 15. D. Mattingly, "Modern tests of lorentz invariance," *Living Rev. Relativ.* **8**(1), 5 (2005).
 16. H. Müller, S. Herrmann, C. Braxmaier, S. Schiller, and A. Peters, "Modern Michelson-Morley experiment using cryogenic optical resonators," *Phys. Rev. Lett.* **91**(2), 020401 (2003).
 17. S. Herrmann, A. Senger, K. Möhle, M. Nagel, E. V. Kovalchuk, and A. Peters, "Rotating optical cavity experiment testing lorentz invariance at the 10^{-17} level," *Phys. Rev. D* **80**(10), 105011 (2009).
 18. C. Braxmaier, H. Müller, O. Pradl, J. Mlynek, A. Peters, and S. Schiller, "Tests of relativity using a cryogenic optical resonator," *Phys. Rev. Lett.* **88**(1), 010401 (2001).
 19. M. E. Tobar, P. Wolf, S. Bize, G. Santarelli, and V. Flambaum, "Testing local lorentz and position invariance and variation of fundamental constants by searching the derivative of the comparison frequency between a cryogenic sapphire oscillator and hydrogen maser," *Phys. Rev. D* **81**(2), 022003 (2010).
 20. C. Braxmaier, T. Schuldt, M. Allab, T. van Zoest, S. Theil, I. Pelivan, S. Herrmann, C. Lämmerzahl, A. Peters, K. Möhle, A. Wicht, M. Nagel, E. Kovalchuk, K. Döringshoff, and H. Dittus, "The space-time asymmetry research (STAR) program," in *EFTF-2010 24th European Frequency and Time Forum*, (2010), pp. 1–8.
 21. A. Milke, D. N. Aguilera, N. Gürlebeck, T. Schuldt, S. F. Herrmann, K. Döringshoff, R. Spannagel, C. Lämmerzahl, A. L. Peters, B. Biering, H. Dittus, and C. Braxmaier, "A space-based optical Kennedy-Thorndike experiment testing special relativity," in *2013 Joint European Frequency and Time Forum and International Frequency Control Symposium (EFTF/IFC)*, (2013), pp. 912–914.
 22. T. Schuldt, S. Saraf, A. Stochino, K. Döringshoff, S. Buchman, G. D. Cutler, J. A. Lipa, S. Tan, J. C. Hanson, B. A. Jaroux, C. Braxmaier, N. Gürlebeck, S. F. Herrmann, C. Lämmerzahl, A. Peters, A. Alfauwaz, A. Alhussien, B. N. Alsuwaidan, T. A. Saud, H. Dittus, U. Johann, S. P. Worden, and R. L. Byer, "mSTAR: Testing special relativity in space using high performance optical frequency references," in *2015 Joint Conference of the IEEE International Frequency Control Symposium and the European Frequency and Time Forum*, (2015), pp. 47–50.
 23. N. Gürlebeck, L. Wörner, T. Schuldt, K. Döringshoff, K. Gaul, D. Gerardi, A. Grenzebach, N. Jha, E. Kovalchuk, A. Resch, T. Wendrich, R. Berger, S. Herrmann, U. Johann, M. Krutzik, A. Peters, E. M. Rasel, and C. Braxmaier, "BOOST: A satellite mission to test Lorentz invariance using high-performance optical frequency references," *Phys. Rev. D* **97**(12), 124051 (2018).
 24. K. Döringshoff, T. Schuldt, E. V. Kovalchuk, J. Stühler, C. Braxmaier, and A. Peters, "A flight-like absolute optical frequency reference based on iodine for laser systems at 1064 nm," *Appl. Phys. B: Lasers Opt.* **123**(6), 183 (2017).
 25. T. Schuldt, K. Döringshoff, E. V. Kovalchuk, A. Keetman, J. Pahl, A. Peters, and C. Braxmaier, "Development of a compact optical absolute frequency reference for space with 10^{-15} instability," *Appl. Opt.* **56**(4), 1101–1106 (2017).
 26. G. Hinshaw, J. L. Weiland, R. S. Hill, N. Odegard, D. Larson, C. L. Bennett, J. Dunkley, B. Gold, M. R. Greason, N. Jarosik, E. Komatsu, M. R. Nolte, L. Page, D. N. Spergel, E. Wollack, M. Halpern, A. Kogut, M. Limon, S. S. Meyer,

- G. S. Tucker, and E. L. Wright, "Five-year Wilkinson microwave anisotropy probe observations: Data processing, sky maps, and basic results," *Astrophys. J., Suppl. Ser.* **180**(2), 225–245 (2009).
27. W. M. Folkner, G. DeVine, W. M. Klipstein, K. McKenzie, D. A. Shaddock, R. E. Spero, R. L. Thompson, D. M. R. Wuchenich, N. Yu, M. Stephens, J. Leitch, M. Davis, J. Decino, C. Pace, and R. B. Pierce, "Laser frequency stabilization for GRACE-II," in *Proceedings of the 2011 Earth Science Technology Forum*, (2011).
 28. R. M. Thompson, W. M. Folkner, G. de Vine, W. M. Klipstein, K. L. Mckenzie, R. E. Spero, Y. N. Sook, M. Stephens, J. G. Leitch, R. Pierce, T. T.-Y. Lam, and D. A. Shaddock, "A flight-like optical reference cavity for GRACE Follow-on laser frequency stabilization," in *2011 Joint Conference of the IEEE International Frequency Control and the European Frequency and Time Forum (FCS) Proceedings*, (2011), pp. 1–3.
 29. K. Numata, A. W. Yu, H. Jiao, S. A. Merritt, F. Micalizzi, M. E. Fahey, J. B. Camp, and M. A. Krainak, "Laser system development for the LISA (Laser Interferometer Space Antenna) mission," in *Proc. SPIE*, vol. 10896 (2019).
 30. K. Nicklaus, M. Herding, X. Wang, N. Beller, O. Fitzau, M. Giesberts, M. Herper, G. P. Barwood, R. A. Williams, P. Gill, H. Koegel, S. A. Webster, and M. Gohlke, "High stability laser for next generation gravity missions," in *Proc. SPIE*, vol. 10563 (2017).
 31. O. Fitzau, P. Betz, P. Cebeci, M. Giesberts, H.-D. Hoffmann, M. Schiemangk, A. Wicht, J. Sanjuan, K. Dahl, S. A. Pyka, E. Kovalchuk, and A. Peters, "Highly stable fiber lasers for satellite-based gravitational measurements," in *Proc. SPIE*, vol. 10897 (2019).
 32. S. Webster and P. Gill, "Force-insensitive optical cavity," *Opt. Lett.* **36**(18), 3572–3574 (2011).
 33. K. Numata, A. Kemery, and J. Camp, "Thermal-noise limit in the frequency stabilization of lasers with rigid cavities," *Phys. Rev. Lett.* **93**(25), 250602 (2004).
 34. T. Kessler, T. Legero, and U. Sterr, "Thermal noise in optical cavities revisited," *J. Opt. Soc. Am. B* **29**(1), 178–184 (2012).
 35. T. Legero, T. Kessler, and U. Sterr, "Tuning the thermal expansion properties of optical reference cavities with fused silica mirrors," *J. Opt. Soc. Am. B* **27**(5), 914–919 (2010).
 36. S. A. Webster, M. Oxborrow, S. Pugla, J. Millo, and P. Gill, "Thermal-noise-limited optical cavity," *Phys. Rev. A* **77**(3), 033847 (2008).
 37. R. W. P. Drever, J. L. Hall, F. V. Kowalski, J. Hough, G. M. Ford, A. J. Munley, and H. Ward, "Laser phase and frequency stabilization using an optical resonator," *Appl. Phys. B: Photophys. Laser Chem.* **31**(2), 97–105 (1983).
 38. J. Sanjuan, N. Gürlebeck, and C. Braxmaier, "Mathematical model of thermal shields for long-term stability optical resonators," *Opt. Express* **23**(14), 17892–17908 (2015).
 39. J. Zhang, W. Wu, X. H. Shi, X. Y. Zeng, K. Deng, and Z. H. Lu, "Design verification of large time constant thermal shields for optical reference cavities," *Rev. Sci. Instrum.* **87**(2), 023104 (2016).
 40. X. Dai, Y. Jiang, C. Hang, Z. Bi, and L. Ma, "Thermal analysis of optical reference cavities for low sensitivity to environmental temperature fluctuations," *Opt. Express* **23**(4), 5134–5146 (2015).
 41. B. D. Dunn, *Materials and processes for spacecraft and high reliability applications* (Springer, 2016).
 42. S. Tan, S. Wang, S. Saraf, and J. A. Lipa, "Pico-Kelvin thermometry and temperature stabilization using a resonant optical cavity," *Opt. Express* **25**(4), 3578–3593 (2017).
 43. T. L. Bergman, A. S. Lavine, F. P. Incropera, and D. P. DeWitt, *Fundamentals of Heat and Mass Transfer* (Wiley, 2011).
 44. P. Hello and J.-Y. Vinet, "Analytical models of transient thermoelastic deformations of mirrors heated by high power cw laser beams," *J. Phys.* **51**(20), 2243–2261 (1990).
 45. S. Häfner, S. Falke, C. Grebing, S. Vogt, T. Legero, M. Merimaa, C. Lisdat, and U. Sterr, " 8×10^{-17} fractional laser frequency instability with a long room-temperature cavity," *Opt. Lett.* **40**(9), 2112–2115 (2015).
 46. D. G. Matei, T. Legero, C. Grebing, S. Häfner, C. Lisdat, R. Weyrich, W. Zhang, L. Sonderhouse, J. M. Robinson, F. Riehle, J. Ye, and U. Sterr, "A second generation of low thermal noise cryogenic silicon resonators," *J. Phys.: Conf. Ser.* **723**, 012031 (2016).
 47. H. Müller, A. Peters, and C. Braxmaier, "Optical fibers with interferometric path length stability by controlled heating for transmission of optical signals and as components in frequency standards," *Appl. Phys. B: Photophys. Laser Chem.* **84**(3), 401–408 (2006).
 48. W. Lewoczko-Adameczyk, M. Schiemangk, H. Müller, and A. Peters, "Thermoacoustic optical path length stabilization in a single-mode optical fiber," *Appl. Opt.* **48**(4), 704–707 (2009).
 49. E. A. Whittaker, M. Gehrtz, and G. C. Bjorklund, "Residual amplitude modulation in laser electro-optic phase modulation," *J. Opt. Soc. Am. B* **2**(8), 1320–1326 (1985).
 50. N. C. Wong and J. L. Hall, "Servo control of amplitude modulation in frequency-modulation spectroscopy: demonstration of shot-noise-limited detection," *J. Opt. Soc. Am. B* **2**(9), 1527–1533 (1985).
 51. H. Shen, L. Li, J. Bi, J. Wang, and L. Chen, "Systematic and quantitative analysis of residual amplitude modulation in pound-drever-hall frequency stabilization," *Phys. Rev. A* **92**(6), 063809 (2015).
 52. J. Bendat, "Statistical errors in measurement of coherence functions and input/output quantities," *J. Sound Vib.* **59**(3), 405–421 (1978).
 53. P.-S. Shaw, T. C. Larason, R. Gupta, S. W. Brown, and K. R. Lykke, "Improved near-infrared spectral responsivity scale," *J. Res. Natl. Inst. Stand. Technol.* **105**(5), 689–700 (2000).
 54. A. Pape, "Hochstabiler Lokaloszillator für einen optischen Magnesium-Frequenzstandard," ph.D. Thesis (Faculty of mathematics and physics, Gottfried Wilhelm Leibniz University, Hannover, 2012).